Astronomy & Astrophysics manuscript no. Heingj3470
April 28, 2020

A He I upper atmosphere around the warm Neptune GJ 3470 b

E. Palle[1,2], L. Nortmann[1,2], N. Casasayas-Barris[1,2], M. Lampón[3], M. López-Puertas[3], J. A. Caballero[4], J. Sanz-Forcada[4], L. M. Lara[3], E. Nagel[5,6], F. Yan[7], F. J. Alonso-Floriano[8], P. J. Amado[3], G. Chen[1,2,9], C. Cifuentes[4], M. Cortés-Contreras[4], S. Czesla[5], K. Molaverdikhani[10], D. Montes[11], V. M. Passegger[5], A. Quirrenbach[12], A. Reiners[7], I. Ribas[13,14], A. Sánchez-López[3], A. Schweitzer[5], M. Stangret[1,2], M. R. Zapatero Osorio[4], and M. Zechmeister[7]

[1] Instituto de Astrofísica de Canarias (IAC), E-38200 La Laguna, Tenerife, Spain
[2] Deptartamento de Astrofísica, Universidad de La Laguna (ULL), E-38206 La Laguna, Tenerife, Spain
[3] Instituto de Astrofísica de Andalucía (IAA-CSIC), Glorieta de la Astronomía s/n, 18008 Granada, Spain
[4] Centro de Astrobiología (CSIC-INTA), ESAC, Camino bajo del castillo s/n, 28692 Villanueva de la Cañada, Madrid, Spain
[5] Hamburger Sternwarte, Universität Hamburg, Gojenbergsweg 112, 21029 Hamburg, Germany
[6] Thüringer Landessternwarte Tautenburg, Sternwarte 5, 07778 Tautenburg, Germany
[7] Institut für Astrophysik, Georg-August-Universität, Friedrich- Hund-Platz 1, 37077 Göttingen, Germany
[8] Leiden Observatory, Leiden University, Postbus 9513, 2300 RA, Leiden, The Netherlands
[9] Key Laboratory of Planetary Sciences, Purple Mountain Observatory, Chinese Academy of Sciences, Nanjing 210033, China
[10] Max-Planck-Institut für Astronomie, Königstuhl 17, 69117 Heidelberg, Germany
[11] Departamento de Física de la Tierra y Astrofísica and IPARCOS-UCM (Intituto de Física de Partículas y del Cosmos de la UCM), Facultad de Ciencias Físicas, Universidad Complutense de Madrid, 28040 Madrid, Spain
[12] Landessternwarte, Zentrum für Astronomie der Universität Heidelberg, Königstuhl 12, 69117 Heidelberg, Germany
[13] Institut de Ciències de l'Espai (ICE, CSIC), Campus UAB, c/ de Can Magrans s/n, 08193 Bellaterra, Barcelona, Spain
[14] Institut d'Estudis Espacials de Catalunya (IEEC), 08034 Barcelona, Spain

Received 13 February 2020 / Accepted 16 April 2020

ABSTRACT

High resolution transit spectroscopy has proven to be a reliable technique for the characterization of the chemical composition of exoplanet atmospheres. Taking advantage of the broad spectral coverage of the CARMENES spectrograph, we initiated a survey aimed at characterizing a broad range of planetary systems. Here, we report our observations of three transits of GJ 3470 b with CARMENES in search of He (2^3S) absorption. On one of the nights, the He I region was heavily contaminated by OH^- telluric emission and, thus, it was not useful for our purposes. The remaining two nights had a very different signal-to-noise ratio (S/N) due to weather. They both indicate the presence of He (2^3S) absorption in the transmission spectrum of GJ 3470 b, although a statistically valid detection can only be claimed for the night with higher S/N. For that night, we retrieved a 1.5±0.3% absorption depth, translating into a $R_p(\lambda)/R_p = 1.15 \pm 0.14$ at this wavelength. Spectro-photometric light curves for this same night also indicate the presence of extra absorption during the planetary transit with a consistent absorption depth. The He (2^3S) absorption is modeled in detail using a radiative transfer code, and the results of our modeling efforts are compared to the observations. We find that the mass-loss rate, $\dot{M}$, is confined to a range of 3×10^{10} g s^{-1} for $T = 6000$ K to 10×10^{10} g s^{-1} for $T = 9000$ K. We discuss the physical mechanisms and implications of the He I detection in GJ 3470 b and put it in context as compared to similar detections and non-detections in other Neptune-size planets. We also present improved stellar and planetary parameter determinations based on our visible and near-infrared observations.

Key words. planetary systems – planets and satellites: individual: GJ 3470b – planets and satellites: atmospheres – methods: observational – techniques: spectroscopic – stars: low-mass

1. Introduction

High resolution spectroscopy has been established over the past few years as a major tool for the characterization of exoplanet atmospheres. The cross-correlation technique of planetary models and observed spectral time series has allowed for the detection of CO, CH_4, and H_2O molecules in the atmospheres of hot Jupiters (Snellen et al. 2010; de Kok et al. 2013; Birkby et al. 2013; Guilluy et al. 2019) and holds the key to spectroscopic characterization of rocky worlds with the upcoming extremely large telescopes (Pallé et al. 2011; Snellen et al. 2013).

Moreover, using high resolution transmission spectroscopy, we are not only able to detect chemical species in the atmosphere of exoplanets, but also to resolve their spectral lines. If the signal-to-noise ratio (S/N) of the final transmission spectrum is high enough, it is possible to obtain temperature and pressure profiles of the upper atmosphere by adjusting isothermal models to different regions of the lines (from core to wings), whose origins reside in different layers of the atmosphere (Wyttenbach et al. 2015, 2017; Casasayas-Barris et al. 2018).

The ability to measure and track line profiles can greatly help in the study of atmospheric escape, which is an important process for understanding planetary physical and chemical evolution. In the past, studies of atmospheric escape relied mostly on space-based observations of the hydrogen Lyα line in the far ultraviolet (Vidal-Madjar et al. 2003), a spectral region with limited access and strongly affected by interstellar absorption.

However, the near-infrared coverage of spectrographs such as CARMENES and GIANO gives access to poorly-explored ex-

oplanet atmospheric features, including the triplet line feature of metastable neutral helium at 10830 Å. This line was proposed as a tracer for atmospheric evaporation in general by Seager & Sasselov (2000) and for particular targets by Oklopčić & Hirata (2018). In this process, intense high-energy irradiation from the host star causes the atmosphere of a hot gas planet to continuously expand resulting in mass flowing away from the planet (Lammer et al. 2013; Lundkvist et al. 2016). With the recent detections of He I with low (Spake et al. 2018) and high resolution spectroscopy (Nortmann et al. 2018; Allart et al. 2018; Salz et al. 2018), it has been proven that this line is a powerful tool for studying the extended atmospheres, mass-loss, and winds in the upper-atmospheres, and for tracking the possible presence of cometary-like atmospheric tails.

Atmospheric erosion by high-energy stellar radiation is believed to play a major role in shaping the distribution of planet radii. Planets with H/He-rich envelopes can be strongly evaporated by stellar irradiation. The evaporation theory predicts the existence of an "evaporation valley" with a paucity of planets at $\sim 1.7\,R_\oplus$ (Seager & Sasselov 2000; Owen & Wu 2013). The radius distribution of small planets ($R_p < 4.0\,R_\oplus$) is bi-modal; small planets tend to have radii of either $\sim 1.3\,R_\oplus$ (super-Earths) or $\sim 2.6\,R_\oplus$ (sub-Neptunes), with a dearth of planets at $\sim 1.7\,R_\oplus$ (Fulton et al. 2017; Van Eylen et al. 2018; Fulton & Petigura 2018). This gap suggests that all small planets might have solid cores, while the cores of sub-Neptune planets are expected to be surrounded by H/He-rich envelopes that significantly enlarge the planetary radii as they are optically thick, while accounting for only 1 % of the total planetary mass. Terrestrial cores can also be surrounded by a thin atmosphere or possess no atmosphere at all, making up the population of super-Earths centered at $R_p \sim 1.3\,R_\oplus$

GJ 3470 b (Bonfils et al. 2012) is a warm Neptune ($R = 3.88 \pm 0.32\,R_\oplus$, $M = 12.58 \pm 1.3\,M_\oplus$), with an equilibrium temperature of 547 K and a period of 3.33 d, located very close to the Neptunian desert. Previous atmospheric studies have inferred a hazy, low-methane or metal-rich atmosphere from *Hubble Space Telescope* observations (Ehrenreich et al. 2014) and a Rayleigh slope in the visible range (Nascimbeni et al. 2013; Chen et al. 2017). While Earth-size and super-Earth planets still remain out of the reach of current instrumental capabilities for evaporation studies, GJ 3470 b is an excellent target for study of such processes. Indeed, Bourrier et al. (2018) already reported the existence of a giant hydrogen exosphere around GJ 3470b and derived a high mass-loss rate. Here we present observations of this target in search for the absorption features of the He (2^3S) triplet. During the process of writing and refereeing of this manuscript, a similar independent work was reported by Ninan et al. (2019).

2. Observations and data analysis

2.1. CARMENES spectroscopy

The transit of GJ 3470 b was observed three times with the CARMENES spectrograph (Quirrenbach et al. 2014, 2018) at the Calar Alto Observatory, on the nights of 16 and 26 December 2018, and on 5 January 2019 (nights 1, 2, and 3, hereafter). CARMENES covers simultaneously the visual (0.52–0.96 μm) and near-infrared (0.96–1.71 μm) spectral ranges with its two channels. A log of the observations, including start and ending times, airmass intervals, and S/Ns can be found in Table 1. Altogether, we collected 13, 14, and 13 in-transit spectra on each night, respectively, using the criteria that at least half the exposure time was taken inside the first and fourth contact interval. Following the same criteria, we also obtained 10, 20, and 22 out-of-transit spectra on nights 1, 2, and 3, respectively.

During the observations, fiber A was fed by the light of the GJ 3470 star and fiber B felt on the sky at about 1.5 arcmin to the target. The spectra of both fibers were extracted from the raw frames using the CARACAL pipeline (Zechmeister et al. 2018). In the standard data flow (Caballero et al. 2016), fiber A spectra are extracted using flat optimized extraction while fiber B spectra are extracted with a simple aperture. Here, we also extracted fiber B with flat optimized extraction so that the spectra of both fibers underwent the same processing scheme.

2.2. Target star parameters

The star GJ 3470 was first cataloged as a high proper motion star in the Luyten-Palomar survey (Luyten 1979). It went almost unnoticed until Bonfils et al. (2012) discovered the transiting planet around it. Since then, and especially with the advent of *Gaia* (Gaia Collaboration et al. 2018), the stellar parameters of GJ 3470 have been better measured.

In Table 2 we compile a comprehensive list of stellar parameters of GJ 3470, either from the literature or derived by us. When there are different published parameter determinations (e.g., spectral type, proper motion), we list the most precise or the most recent ones.

We determined the photospheric parameters $T_{\rm eff}$, $\log g$, and [Fe/H] following the methods described by Passegger et al. (2019), using the combined VIS+NIR spectra of the two CARMENES channels. The physical stellar parameters L, R, and M were determined following Schweitzer et al. (2019), i.e., we measured the luminosity L by using the *Gaia* DR2 parallax and integrated multi-wavelength photometry from B to $W4$, applied Stefan-Boltzmann's law to obtain the radius R, and, finally, used the linear mass-radius relation from Schweitzer et al. (2019) to arrive at the mass M.

Our photospheric parameters ($T_{\rm eff}$, $\log g$, and [Fe/H]) are consistent with Demory et al. (2013). Their mass was based on the empirical mass-magnitude relation of Delfosse et al. (2000) and, hence, it differs by the same amount from our value as results from Delfosse et al. (2000) differ from the updated mass-magnitude relation of Mann et al. (2019). Our method, however, agrees very well with the updated mass-magnitude relation (c.f., Schweitzer et al. 2019). The radii determination of Demory et al. (2013) or Awiphan et al. (2016), however, were based on the average density inside the planetary orbit, which added an additional uncertainty.

In addition, we also used the latest astrometric and absolute radial velocity data of *Gaia* for determining Galactocentric space velocities UVW and assigning GJ 3470 to the Galactic young disc population. We estimated a stellar age between 0.6 Ga and 3.0 Ga, which is consistent with its kinematic population, the presence of Hα in absorption (in spite of its M2.0 V spectral type), the faint Ca II H&K emission, the relatively slow rotation (quantified by the low rotational velocity and long rotational period), and its weak X-ray emission, as well as with previous determinations in the literature (e.g., Bourrier et al. 2018; Bonfils et al. 2012).

We also searched the literature for additional information on GJ 3470. What was of particular interest is the i'- and z'-band lucky imaging of the star by Wöllert & Brandner (2015), who derived upper limits on the existence of targets brighter than $\Delta z' \approx 4.0$ mag and 6.0 mag at 0.25 arcsec and 5 arcsec, respectively. These limits translated into the absence of objects at the

Table 1. Observing log of the GJ 3470 b transit observations. RV is the averaged barycentric Earth radial velocity during the night.

Night t	Date	Start UT	End UT	t_{exp} [s]	N_{obs}	Airmass	S/N	RV [km/s]
1	2018 Dec 16	22:23	02:05	498	23	1.85→1.08→1.08	26	7.15
2	2018 Dec 26	21:38	03:13	498	34	1.9→1.079→1.136	66	12.24
3	2019 Jan 05	21:54	03:27	498	35	1.48→1.078→1.25	61	16.90

Table 2. Stellar parameters of GJ 3470.

Parameter	Value	Reference
Name and identifiers		
Name	LP 424–4	Luy79
GJ	3470	GJ91
Karmn	J07590+153	AF15
Key parameters		
α	07:59:05.84	*Gaia* DR2
δ	+15:23:29.2	*Gaia* DR2
G (mag)	11.3537±0.0013	*Gaia* DR2
J (mag)	8.794±0.026	2MASS
Spectral type	M2.0 V	Lep13
Parallax and kinematics		
π (mas)	33.96±0.06	*Gaia* DR2
d (pc)	29.45±0.05	*Gaia* DR2
$\mu_\alpha \cos\delta$ (mas a^{-1})	–185.73±0.11	*Gaia* DR2
μ_δ (mas a^{-1})	–57.26±0.06	*Gaia* DR2
V_r (km s^{-1})^a	+26.5169±0.0005	Bou18
U (km s^{-1})	–32.04±0.21	This work
V (km s^{-1})	–12.42±0.10	This work
W (km s^{-1})	–15.37±0.10	This work
Kinematic population	Young disc	This work
Photospheric parameters		
$T_{\rm eff}$ (K)	3725±54	This work
log g	4.65±0.06	This work
[Fe/H]	+0.420±0.019	This work
$v \sin i$ (km s^{-1})	$\lesssim$2	Bon12
Physical parameters		
L (10^{-4} $L_\odot$)	390±5	This work
R ($R_\odot$)	0.474±0.014	This work
M ($M_\odot$)	0.476±0.019	This work
Age (Ga)	0.6–3.0	This work
Other parameters		
$P_{\rm rot}$ (d)	20.70±0.15	Bid15
pEW(Hα) (Å)	+0.39±0.09	Gai14
log $R'_{\rm HK}$	–4.91±0.11	SM15
$F_{5-100\,\text{Å}}$ (10^{27} erg s^{-1})	2.3	Bou18
$F_{100-504\,\text{Å}}$ (10^{27} erg s^{-1})	2.7	Bou18

References. AF15: Alonso-Floriano et al. (2015); Bid14: Biddle et al. (2014); Bon12: Bonfils et al. (2012); Bou18: Bourrier et al. (2018); Gai14: Gaidos et al. (2014); GJ91: Gliese & Jahreiß (1991); Lép13: Lépine et al. (2013); Luy79: Luyten (1979); SM15: Suárez Mascareño et al. (2015); 2MASS: Skrutskie et al. (2006); *Gaia* DR2: Gaia Collaboration et al. (2018). **Notes.** ^{a} Soubiran et al. (2018) tabulated V_r = +26.341±0.004 km s^{-1}, but their uncertainties did not include gravitational redshift or photospheric convection.

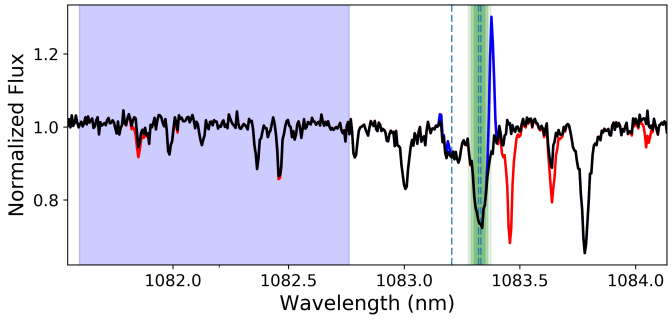

Fig. 1. Zoom of one CARMENES spectrum of GJ 3470 in the wavelength region containing the He I triplet. In red the raw spectra after standard data reduction is plotted. Over-plotted in blue is the same spectrum after removal of the telluric features (mainly water in this region) using `molecfit`. In black is the same spectrum after adjusting and removing also the OH$^-$ spectral features. In the figure, the wavelength region used to normalize the continuum of all spectra is marked with a blue shade, and the region around the He I line cores used to calculate the spectro-photometric transit light curves is marked with a shaded green region.

substellar boundary at separations beyond 150 au and more massive than 0.1 $M_\odot$ down to 7 au, approximately.

For the system parameters, throughout the rest of the paper, we adopt the stellar velocity semi-amplitude $K_{\rm star}$ from Bonfils et al. (2012). For the planet parameters, we recalculated here the radius, mass, density, and equilibrium temperature values (see Table 4) based on the stellar parameters of Table 2. The remaining values were taken from Bourrier et al. (2018) and references therein. We calculated the velocity semi-amplitude of the planet $K_{\rm planet}$ from these values.

2.3. Telluric absorption removal

The He I λ10830 Å triplet is contaminated by telluric absorption from atmospheric water vapor and OH$^-$ emission (Nortmann et al. 2018; Salz et al. 2018). Due to the Earth's barycentric velocity, the relative position between the He I and the telluric features varies with date. To detect the weak planetary signals in the spectral time series, the telluric contribution needs to be removed from the spectra.

The water vapor removal in each individual spectrum was performed with `molecfit`, which fits synthetic transmission models to the observations (Smette et al. 2015; Kausch et al. 2015). To adapt the telluric model to the spectra, `molecfit` allows the user to convolve the model with an instrumental profile. We analyzed several thousand lines from hollow cathode lamp spectra, which are regularly used as calibration sources, and measured the Gaussian and Lorentzian FWHM components. Based on our analysis, we adopted a value of 5.26 pixel and 0.75 pixel for the Gaussian and the Lorentzian FWHM components, respectively. The determination of the instrumental line spread function is described in more detail in Nagel et al. (sub-

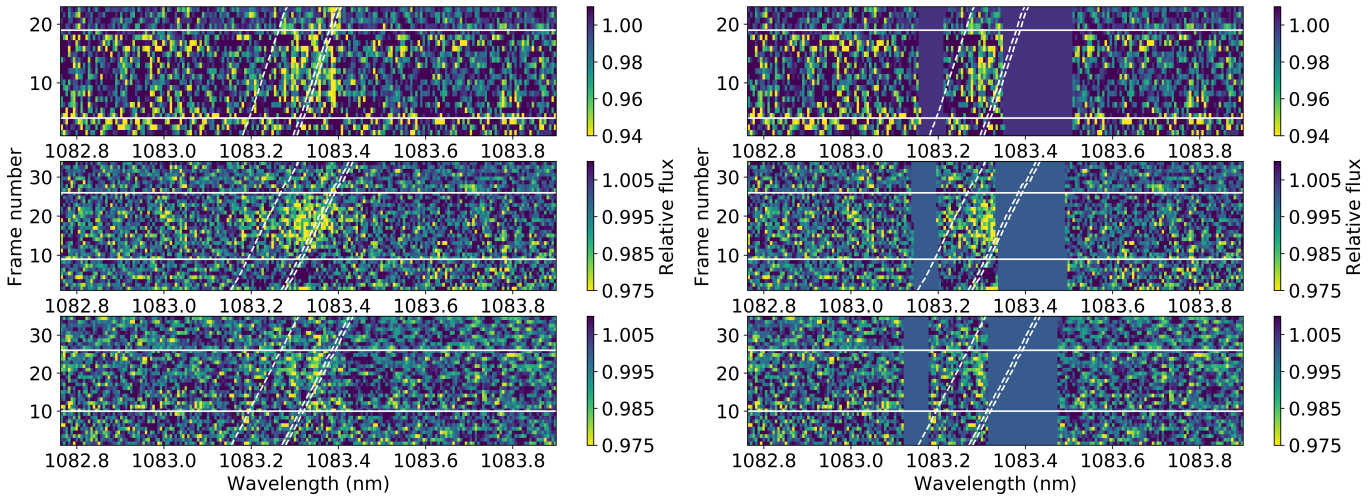

Fig. 2. Observed 2D residual maps after dividing each spectrum by the master-out spectrum. Form top to bottom are nights 1, 2 and 3, respectively. The data on the right and left panels are exactly the same, but in the right panel, the regions affected by OH^- contamination are masked to illustrate the amount of usable data for each night. The maps comprise the region around the He I triplet, and are shown in the stellar rest frame. The horizontal white bars mark the beginning (T1) and end (T4) of the transit. The tilted dashed lines mark the expected planetary trail of triplet. Note the different color scale between night 1 and nights 2 and 3.

mitted). The effect of telluric line removal is illustrated in Figure 1.

The He I triplet lines were also located between OH^- emission lines (see also Fig. 1), which are not accounted for by `molecfit`. These lines were also observed in the spectra obtained from fiber B, which was pointed at the sky. We corrected the emission lines in fiber A by first modeling the lines in fiber B and then subtracting the model from the spectra of fiber A. In fiber B there was no detectable contamination from the stellar spectra. To construct the model, we first obtained a master spectrum for fiber B, calculated by summing up all fiber B spectra for a given night. To this spectrum, we fitted a Voigt profile to the fiber B OH^- line redwards of the stellar He I lines, and two Gaussian profiles (with the same amplitude and width) to the two weakest OH^- lines bluewards of the stellar He I lines. The amplitude of the fit to the strongest OH^- emission could vary for every fiber B spectrum independently, but we kept the values for the positions, widths, and amplitude ratios between strong and weak OH^- lines fixed for all the spectra of a given night. When allowing the widths of the lines to vary, we found no statistically significant differences in the final results. Finally, when subtracting the model fit of fiber B from fiber A, we applied a scaling factor (0.88 ± 0.05) to the model to compensate for the efficiency differences between the two fibers. This factor was calculated from a high S/N observation with CARMENES, and was fixed for all spectra and nights. The error of this factor had no significant impact on our results compared to the standard deviation.

3. Results

3.1. He I transmission spectra

After correction of the telluric absorption and emission, we normalized all spectra by the mean value of the region between 10815.962 Å and 10827.624 Å in vacuum. This region, which lies blue-wards of the He I lines, was almost unaffected by telluric absorption and, therefore, gave a robust reference level for the pseudo-continuum (see Fig. 1).

After normalization we aligned all the spectra to the stellar rest frame. We then calculated a master out-of-transit spectrum by computing the mean spectrum of all spectra obtained out of transit, and divided each individual spectrum (in and out) by this master. This technique has been previously applied in several works (Wyttenbach et al. 2015; Salz et al. 2018; Casasayas-Barris et al. 2018). After removal of the stellar signal, the residual spectra should contain the possible atmospheric planetary signal that, in the stellar rest frame, moves through wavelength space as time progresses, from blue-shifted at the beginning of the transit to red-shifted towards the end. To obtain the transmission spectrum, we aligned these residual spectra to the planet rest frame and calculated the mean in-transit spectrum between the second and third contacts.

In Figure 2 (left panels) the residual maps around the He I triplet are shown for each of the three nights. Also plotted are the ingress start time (first contact) and egress end time (fourth contact), as well as the expected residual trace of a possible planetary signal. Significant positive residual indicative of He I absorption was visible for night 2, but not for the other two nights. The lack of reproducible results could be indicative of a spurious signal. However, it was not clear that this was the case. For night 1, the S/N of the measurements was low due to weather conditions (see Table 1), and while a positive signal was also seen at the expected He I wavelengths, the data quality did not allow the signal to reach the 3σ significance level required to claim a detection.

For night 3, which had a S/N as night 2, the problem was the contamination of the He I signal by telluric OH^- lines. During the night, the position of the OH^- lines with respect to the He lines changed. To illustrate this, we plot in Figure 2 (right panels) the same residual maps. In this figure, however, the spectral regions that during the transit (T1-T4) were overlapping with OH^- lines were masked. It is readily appreciable from the figure that night 3 had the largest OH^- contamination, with practically no unaffected signal from the planet. Thus, we kept the analysis of that night for completeness, but a He I signal detection was not expected for that night even if the planetary absorption was there.

Figure 3 shows the transmission spectrum of He I derived for each of the three nights. The transmission spectrum was calculated in two different ways. The first was by simply masking the OH-affected regions of the spectrum. It is plotted in the figure in black, and it is discontinuous in these affected regions. A second way to calculate the spectra was to correct for OH^- contamination, as described in Section 2.1. These spectra are over-plotted in red and nothing is masked. The corrected and uncorrected spectra were identical in the common regions.

In summary, we concluded from the figure that both nights 1 and 2 showed strong absorption features centered in the He I λ 10830 Å triplet. While the scatter for night 1 was large due to the low S/N of the observations, the absorption was clear for night 2, reaching 1.5±0.3 %. Following Nortmann et al. (2018), and using the values in Tables 1 and 2, this translated into a planetary radius increase of $R_p(\lambda)/R_p = 1.15 \pm 0.14$, or an equivalent scale height of $\Delta R_p/H_{eq} = 77 \pm 9$.

The absorption in night 1 nearly doubled that of night 2, but there were strong residual features in the transmission spectrum, at the few percent level, that were probably associated to low S/N systematics and were affecting the absorption depth. Night 3, represented at the same scale as night 2, did not show any significant absorption feature. The nightly retrieved absorption depths from the transmission spectrum and the transit light curves (see next section) are given in Table 3.

3.2. Spectro-photometric light curves

Spectro-photometric light curves from the spectral data were useful to understand if the absorption features had a temporal variability compatible with the planetary transit. Thus, in order to monitor the temporal behavior of the excess He I absorption, we calculated the transit light curves for this line. To do this, we integrated the counts in band-passes of three different widths (0.40, 0.74, and 0.97 Å) centered on the two deepest lines of the He I triplet. This integration was done in the planet rest frame. The summation intervals are marked in Figure 1. The methodology that we followed to build the spectro-photometric light curves was described by Nortmann et al. (2018) and Casasayas-Barris et al. (2019). For GJ 3470 b, the Rossiter-McLaughlin effect on the transmission spectrum and photometric light curves is expected to be negligible.

In Figure 4 we plot the transit light curves for the He (2^3S) absorption for each of the three nights. As in the case of the transmission spectrum, a clear transit was detected only on night 2, while the light curves for nights 1 and 3 were mainly flat. The error bars took into account the individual scatter of each spectrum and the number of points integrated. For night 1, there were a few outliers that coincided in time with ingress and egress, and may resemble of a transit feature, but there was no statistically significant additional absorption during transit. Given the low S/N of the data, this was not surprising as the construction of spectro-photometric light curves from high-dispersion spectroscopy requires a higher S/N (Casasayas-Barris et al. 2020). The non-detection of a transit signal for night 3 was consistent with the flat transmission spectrum for the same night.

For the clear transit of night 2, we observed a transit duration roughy coincident with the expected ingress and egress times. The retrieved depth of the transit was consistent with that retrieved from the transmission spectrum analysis (Table 3). An extra absorption extending further than the egress (tail structure) might be present, but it was not statistically significant within our error bars. New observations minimizing OH^- emission contamination and with larger telescopes will be needed to explore this issue. For night 2 we also observed an "emission-like" feature just before the transit, which is already visible in the 2D residual maps in Figure 2 as a dark blue region just before the transit start. Currently, we have no explanation for this.

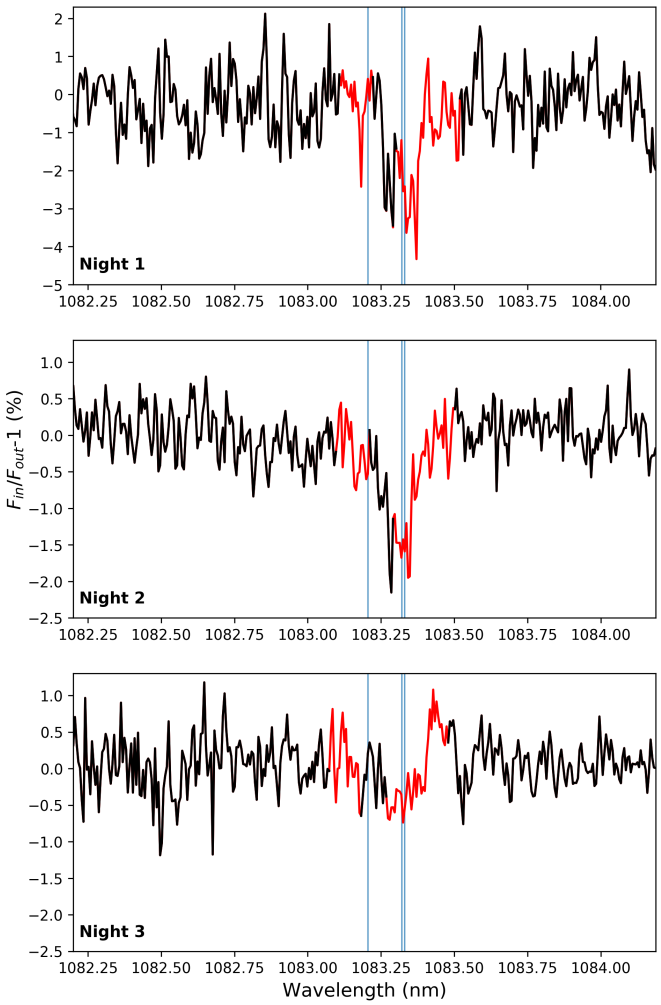

Fig. 3. Mid-transit (T2-T3) transmission spectrum around the HeI triplet for night 1, 2 and 3, from top to bottom, respectively. The black line shows the spectral regions unaffected by OH^- lines, while the red line marks the spectral regions affected, and corrected for, OH^- emission. The blue vertical lines mark the helium triplet line center positions. Note the different absorption scale between night 1 and nights 2 and 3.

4. Modeling the He I absorption

As previously done in the case of HD 209458 b (Alonso-Floriano et al. 2019), we modeled here the He (2^3S) absorption of GJ 3470 b. Briefly, we used a one-dimensional hydrodynamic and spherically symmetric model together with a non-local thermodynamic equilibrium (non-LTE) model to calculate the He (2^3S) density distribution in the upper atmosphere of the planet (Lampón et al. 2020). The hydrodynamic equations were solved assuming that the escaping gas has a constant speed of sound, $v_s = \sqrt{k\,T/\mu}$, where k is the Boltzmann constant, T is temperature, and μ in the mean molecular weight. This assumption leads to the same analytical solution as the isothermal Parker wind solution. However, the atmosphere is not isothermal. Instead the temperature is such that the T/μ ratio is constant with

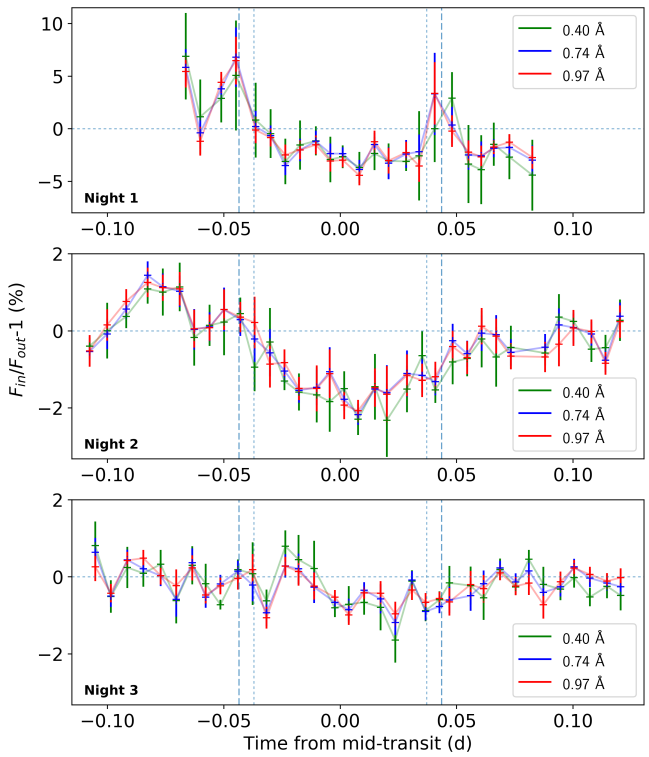

Fig. 4. Spectro-photometric light curves of the He (2^3S) absorption of the transit of GJ 3470 b for each of the three nights: 1 to 3 from top to bottom, respectively. The light curves have been constructed using three different wavelength integration intervals: 0.40 Å (green), 0.74 Å (blue), and 0.97 Å (red). Note the different absorption scale between night 1 and nights 2 and 3.

Table 3. Comparison table of absorption depths retrieved for each individual night[a].

Night	TS	TS-Nc	LC
1	2.4 ± 0.9	3.5 ± 0.9	2.1 ± 0.9
2	1.5 ± 0.3	2.2 ± 0.3	1.4 ± 0.5
3	0.4 ± 0.2	...	0.4 ± 0.3

Notes. [(a)] TS means the value retrieved from the averaged absorption over a 0.4 Å-wide bin (green shadow in Figure 1). TS-Nc is the same calculation over the transmissions spectrum without accounting for OH-corrected regions (i.e., considering black points only). LC refers to the absorption depth retrieved from the transit light curves between second (T2) and third (T3) contacts. For the transmission spectrum the error is simply calculated as the rms over the continuum region 1082.5–1083 nm.

altitude, that is, $v_s = \sqrt{kT/\mu} = \sqrt{kT_0/\bar{\mu}}$, where $\bar{\mu}$ is the average mean molecular weight calculated in the model, and T_0 is a model input parameter that is very similar to the maximum of the thermospheric temperature profile calculated by hydrodynamic models that solve the energy balance equation (see, e.g., Salz et al. 2016). The He (2^3S) absorption was later computed by using a radiative transfer code for the standard primary transit geometry (Lampón et al. 2020). The absorption coefficients and wavelengths for the three metastable He I lines were taken from the NIST Atomic Spectra Database[1]. Doppler line shapes were assumed at the atmospheric temperature used in the helium model density, and an additional broadening produced by turbulent velocities was included as described in the reference above. The component of the radial velocity of the gas along the line of sight (towards the observer, i.e., arising from the planet day- and night-sides around the terminator) was also included in order to account for the motion of He (2^3S) as predicted in the hydrodynamic model. From the modeling results, we found that the He (2^3S) distribution is significantly more extended than in the case of HD 209458 b. Hence, we found it necessary to perform the integration of the He (2^3S) absorption up to 10 R_P.

Figure 5 shows the observed transmission spectrum of night 2, together with a calculation performed with the model described above for an effective temperature of 6000 K and a substellar mass-loss-rate of 3×10^{10} g s^{-1}.

The inclusion of the broadening of the lines due to turbulence ($v_{\rm turb} = \sqrt{5kT/3m}$, where m is the mass of a helium atom), in addition to the standard Doppler broadening, was not enough to explain the measured broadening in the observations (cyan line in Fig. 5). However, when we included the broadening due to the component of the radial velocities of the gas calculated in our model along the observer's line of sight, (see Eq. 15 in Lampón et al. 2020), then we were able to explain the absorption line width (red curve in Fig. 5). Because of the weak surface gravity of this planet, the obtained radial velocities were rather large, even at relatively short radii. In particular, we obtained radial velocities in the range of 5 to 20 km s^{-1} for r = 1–10 R_P. These velocities, particularly at low radii, induce a rather significant broadening as shown in Fig. 5. Nevertheless, we observed that the peak of the absorption was slightly shifted to blue wavelengths, indicating that there may be a net blue wind flowing from the day to the night side, for which we estimated a net velocity shift of –3.2±1.3 km s^{-1}. This result is similar to that of –1.8 km s^{-1} found by Alonso-Floriano et al. (2019) for HD 209458b, which was also interpreted as a net day-to-night thermospheric wind. Our model, being 1D and spherically homogeneous, was not able to predict any net blue or red component. Hence, the calculation shown in Fig. 5 (red curve) was obtained by imposing a net shift of –3.2 km s^{-1} on the radial velocities computed by our model.

Our 1D hydrodynamic and spherically symmetric model was based on the assumption of a constant sound speed and, hence, it was unable to discriminate among the temperature and the mass-loss rate. That is, both quantities are degenerate. However, it had the advantage of being computationally very efficient, which allowed us to explore a wide range of atmospheric temperatures and mass-loss rates that were compatible with the He (2^3S) absorption. Hence, this measurement significantly constrained the parameter space of those quantities. We performed calculations by covering a range of maximum temperatures from 6000 K to 9000 K and found that the mass-loss rate, $\dot{M}$, is confined to a range of 3×10^{10} g s^{-1} for T = 6000 K to about 10×10^{10} g s^{-1} for T = 9000 K .

For HD 209458 b, Lampón et al. (2020) derived mass-loss rates of 1.3×10^{10} g s^{-1} and 1.3×10^{11} g s^{-1} for those temperatures (derived for a H/He ratio of 98/2), which are slightly smaller at about 6000 K but slightly larger at a temperature of 9000 K than those derived here for GJ 3470 b for the canonical H/He ratio of 90/10. However, if considering the same H/He ratio, the mass-loss rates are about a factor of 10 larger in GJ 3470 b than in HD 209458 b.

The mass-loss rate of GJ 3470 b derived by Bourrier et al. (2018) was in the range of (1.5–8.5) $\times 10^{10}$ g s^{-1}. The lower limit was derived assuming the mass-loss rate of only neutral hydrogen atoms (that is, neither H^+ nor helium were included), while

[1] https://www.nist.gov/pml/atomic-spectra-database

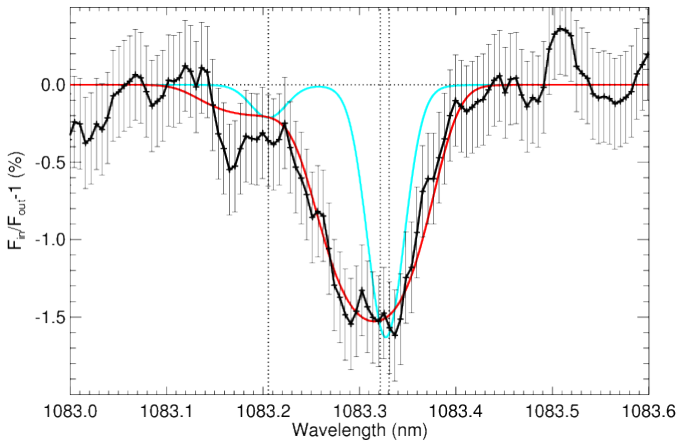

Fig. 5. Transmission spectrum of the He I triplet during transit. Measured absorption (+), and their respective estimated errors, are shown in black. The data are the same as in Fig. 3 but with a three-point running mean applied. The cyan curve shows the absorption profile when only the Doppler and turbulence broadenings are included. The red curve is the best-fit model obtained for an effective temperature of 6000 K, a mass-loss rate ($\dot{M}$) of 3×10^{10} g s^{-1} and a H/He mole-fraction ratio of 90/10. This calculation included, in addition to the Doppler and turbulence broadenings, the broadening induced by the radial velocities of the model and an additional blue net wind of –3.2 km s^{-1}. The positions of the three He I lines are marked by vertical dotted lines.

the upper limit was obtained by using the energy-limited approach. Our value at 6000 K is about twice their lower limit, but both are consistent since they only include neutral hydrogen. Our rate at a temperature of 9000 K is slightly larger than their upper limit.

5. Discussion and conclusions

Here we report the detection of He I absorption in the upper atmosphere of GJ 3470 b. To understand this observation in a broader context, it is important to compare the properties of GJ 3470 b with two other well-studied Neptune planets: GJ 436 b (Butler et al. 2004; Gillon et al. 2007) and HAT-P-11 b (Bakos et al. 2010). All three planets have very close radius values (see Table 4, where the physical properties of all three planets are summarized). GJ 436 b and HAT-P-11 b have also nearly the same mass, density, and age (Demory et al. 2013; Fraine et al. 2014), while GJ 3470 b is less massive and only about half the average bulk density.

For GJ 436 b, very significant extra absorption during transit has been observed in Lyα. Both Kulow et al. (2014) and Ehrenreich et al. (2015) detected an extended transit with a comet-like tail structure, reaching a depth of almost 50 % of the stellar flux. Despite this, absorption in Hα during transit has not been detected, and Cauley et al. (2017) suggested that the large cloud of neutral hydrogen surrounding GJ 436 b is almost entirely in the ground state. While a strong absorption in He (2^3S) was theoretically predicted by Oklopčić & Hirata (2018), Nortmann et al. (2018) found no detectable evidence for it. However, Salz et al. (2016) showed that the concentration of ionized hydrogen in GJ 436 b is significantly lower than in GJ 3470 b at high altitudes (at radii larger than $\sim3R_P$, the region where according to our model the He (2^3S) is mainly formed). We recall that the major formation process of He (2^3S) is recombination from $He^+ + e^-$. Thus, a lower density of ionized hydrogen leads to a lower electron concentration and, consequently, to a less efficient He (2^3S) formation, which is in line with the observations of Nortmann et al. (2018). In the case of HAT-P-11 b, there are no published detections of extra absorption either in Hα or Lyα, but Allart et al. (2018) detected a strong signature of He (2^3S) absorption during transit.

For GJ 3470 b, based on ultraviolet observations of the Lyα absorption, Bourrier et al. (2018) estimated a mass-loss rate of $(1.5–8.5)\times10^{10}$ g s^{-1}, comparable to that of hot Jupiters, and concluded that the planet could already have lost up to 40 % of its mass over its 2 Gyr lifetime. This observation is roughly in line (depending on the actual thermospheric temperature) with the $\dot{M}$ derived from our analysis of the observed He (2^3S) absorption described above. We obtained a value of $(3–10)\times10^{10}$ g s^{-1} for a temperature range of 6000 K to 9000 K. Those values are also comparable to the ones obtained by Lampón et al. (2020) for He (2^3S) $\dot{M}$ of the hot Jupiter HD 209458 b. We caution, however, that there is a strong dependency of these values on the assumed H/He ratio values, which are currently unknown. Lampón et al. (2020) derived similar mass-loss rate by using H/He = 98/2, imposed by the Lyα measurements, but they had large errors as only the wings of the line were detected. If we used only the He (2^3S) measurements and assumed the same H/He = 90/10 for both HD 209458 b and GJ 3470 b, then the mass-loss rate of GJ 3470 b would be about a factor 10 larger than caculated in Sect. 4.

It is of particular interest to consider why planets with such similar physical properties display very different upper atmospheric escape properties. As discussed in Nortmann et al. (2018), the formation of the He I λ10830 Å triplet in exoplanet atmospheres is directly linked to the stellar irradiation with $\lambda <$ 504 Å, which ionizes the neutral helium atoms, with a subsequent recombination with electrons. Therefore, it is essential to know the X-ray and extreme ultraviolet (XUV) irradiation in this spectral range. The X-ray observations of GJ 3470 reveal a moderately active star ($\log L_X/L_{bol} = -4.8$) with some flaring variability (J. Sanz-Forcada et al. in prep). The analysis of the X-ray spectrum and ultraviolet lines was used to construct a coronal model and calculate a spectral energy distribution in the full range 1–1200 Å (Bourrier et al. 2018, and Sanz-Forcada et al. in prep.). The XUV luminosity in the 5–504 Å range is $L_{XUV\ He} = 5\times10^{27}$ erg s^{-1}, yielding an irradiation in this band at the distance of GJ 3470 b of $f_{XUV\ He} = 1435$ erg s^{-1} cm^{-2}. Thus, the $f_{XUV,He}$ of GJ 3470 b is similar to that of HAT-P-11 b, but it is almost one order of magnitude larger than that of GJ 436 b (Table 4). While the youth and lower density of GJ 3470 b compared to the other two Neptunes surely plays a role, our results suggest that He (2^3S) ionization is mainly driven by XUV stellar irradiation.

As mentioned above, we previously analyzed the He (2^3S) absorption detection in the hot Jupiter HD 209458 b (Alonso-Floriano et al. 2019; Lampón et al. 2020), another CARMENES target of our He I survey. We noticed two significant differences. First, the He (2^3S) absorption profile of GJ 3470 b is significantly wider than in HD 209458 b. Secondly, our model showed that the absorption in GJ 3470 b takes place mainly in the outer regions. Both facts suggest that GJ 3470 b has a rather expanded atmosphere with strong winds prevailing in its upper thermosphere. These results are in line with its lower gravity with respect to HD 209458 b. Moreover, we found that the $\dot{M}$/T relationship derived from the measured He (2^3S) absorptions are rather different: GJ 3470 b exhibits comparable or even larger $\dot{M}$ (for the

same temperature) than the hot Jupiter HD 209458 b. These results suggest that escape of GJ 3470 b is possibly driven by a different process than in HD 209458 b.

Acknowledgements. CARMENES is an instrument for the Centro Astronómico Hispano-Alemán (CAHA) at Calar Alto (Almería, Spain), operated jointly by the Junta de Andalucía and the Instituto de Astrofísica de Andalucía (CSIC). CARMENES was funded by the German Max-Planck-Gesellschaft (MPG), the Spanish Consejo Superior de Investigaciones Científicas (CSIC), the European Union through FEDER/ERF FICTS-2011-02 funds, and the members of the CARMENES Consortium. We acknowledge financial support from the Agencia Estatal de Investigación of the Ministerio de Ciencia, Innovación y Universidades and the European FEDER/ERF funds through projects ESP2016-80435-C2-2-R, ESP2016-76076-R, and BES-2015-074542, and AYA2016-79425-C3-1/2/3-P, the Deutsche Forschungsgemeinschaft through the Research Unit FOR2544 "Blue Planets around Red Stars" and the Priority Program SPP 1992 "Exploring the Diversity of Extrasolar Planets" RE 1664/16-1, the National Natural Science Foundation of China through grants 11503088, 11573073, and 11573075, and the Natural Science Foundation of Jiangsu Province through grant BK20190110. Finally, we wish to thank Dr. Vincent Bourrier and an anonymous referee for discussion and comments that helped to improve the contents of this manuscript.

References

Allart, R., Bourrier, V., Lovis, C., et al. 2018, Science, 362, 1384
Alonso-Floriano, F. J., Morales, J. C., Caballero, J. A., et al. 2015, A&A, 577, A128
Alonso-Floriano, F. J., Snellen, I. A. G., Czesla, S., et al. 2019, A&A, 629, A110
Awiphan, S., Kerins, E., Pichadee, S., et al. 2016, MNRAS, 463, 2574
Bakos, G. Á., Torres, G., Pál, A., et al. 2010, ApJ, 710, 1724
Biddle, L. I., Pearson, K. A., Crossfield, I. J. M., et al. 2014, MNRAS, 443, 1810
Birkby, J. L., de Kok, R. J., Brogi, M., et al. 2013, MNRAS, 436, L35
Bonfils, X., Gillon, M., Udry, S., et al. 2012, A&A, 546, A27
Bourrier, V., Lecavelier des Etangs, A., Ehrenreich, D., et al. 2018, A&A, 620, A147
Butler, R. P., Vogt, S. S., Marcy, G. W., et al. 2004, ApJ, 617, 580
Caballero, J. A., Guàrdia, J., López del Fresno, M., et al. 2016, Society of Photo-Optical Instrumentation Engineers (SPIE) Conference Series, Vol. 9910, CARMENES: data flow, 99100E
Casasayas-Barris, N., Pallé, E., Yan, F., et al. 2018, A&A, 616, A151
Casasayas-Barris, N., Pallé, E., Yan, F., et al. 2019, A&A, 628, A9
Casasayas-Barris, N., Pallé, E., Yan, F., et al. 2020, A&A, 635, A206
Cauley, P. W., Redfield, S., & Jensen, A. G. 2017, AJ, 153, 81
Chen, G., Guenther, E. W., Pallé, E., et al. 2017, A&A, 600, A138
de Kok, R. J., Brogi, M., Snellen, I. A. G., et al. 2013, A&A, 554, A82
Delfosse, X., Forveille, T., Ségransan, D., et al. 2000, A&A, 364, 217
Demory, B.-O., Torres, G., Neves, V., et al. 2013, ApJ, 768, 154
Dragomir, D., Benneke, B., Pearson, K. A., et al. 2015, ApJ, 814, 102
Ehrenreich, D., Bonfils, X., Lovis, C., et al. 2014, A&A, 570, A89
Ehrenreich, D., Bourrier, V., Wheatley, P. J., et al. 2015, Nature, 522, 459
Fraine, J., Deming, D., Benneke, B., et al. 2014, Nature, 513, 526
Fulton, B. J. & Petigura, E. A. 2018, AJ, 156, 264
Fulton, B. J., Petigura, E. A., Howard, A. W., et al. 2017, AJ, 154, 109
Gaia Collaboration, Brown, A. G. A., Vallenari, A., et al. 2018, A&A, 616, A1
Gaidos, E., Mann, A. W., Lépine, S., et al. 2014, MNRAS, 443, 2561
Gillon, M., Pont, F., Demory, B. O., et al. 2007, A&A, 472, L13
Gliese, W. & Jahreiß, H. 1991, Preliminary Version of the Third Catalogue of Nearby Stars, Tech. rep.
Guilluy, G., Sozzetti, A., Brogi, M., et al. 2019, A&A, 625, A107
Kausch, W., Noll, S., Smette, A., et al. 2015, A&A, 576, A78
Kosiarek, M. R., Crossfield, I. J. M., Hardegree-Ullman, K. K., et al. 2019, AJ, 157, 97
Kulow, J. R., France, K., Linsky, J., & Loyd, R. O. P. 2014, ApJ, 786, 132
Lammer, H., Erkaev, N. V., Odert, P., et al. 2013, MNRAS, 430, 1247
Lampón, M., López-Puertas, M., Lara, L. M., et al. 2020, A&A, 636, A13
Lépine, S., Hilton, E. J., Mann, A. W., et al. 2013, AJ, 145, 102
Lundkvist, M. S., Kjeldsen, H., Albrecht, S., et al. 2016, Nature Communications, 7, 11201
Luyten, W. J. 1979, New Luyten catalogue of stars with proper motions larger than two tenths of an arcsecond; and first supplement; NLTT. (Minneapolis (1979)); Label 12 = short description; Label 13 = documentation by Warren; Label 14 = catalogue
Mann, A. W., Dupuy, T., Kraus, A. L., et al. 2019, ApJ, 871, 63
Nascimbeni, V., Piotto, G., Pagano, I., et al. 2013, A&A, 559, A32
Ninan, J. P., Stefansson, G., Mahadevan, S., et al. 2019, arXiv e-prints, arXiv:1910.02070
Nortmann, L., Pallé, E., Salz, M., et al. 2018, Science, 362, 1388
Oklopčić, A. & Hirata, C. M. 2018, ApJ, 855, L11
Owen, J. E. & Wu, Y. 2013, ApJ, 775, 105
Pallé, E., Zapatero Osorio, M. R., & García Muñoz, A. 2011, ApJ, 728, 19
Passegger, V. M., Schweitzer, A., Shulyak, D., et al. 2019, A&A, 627, A161
Quirrenbach, A., Amado, P. J., Caballero, J. A., et al. 2014, in Proc. SPIE, Vol. 9147, Ground-based and Airborne Instrumentation for Astronomy V, 91471F
Quirrenbach, A., Amado, P. J., Ribas, I., et al. 2018, in Society of Photo-Optical Instrumentation Engineers (SPIE) Conference Series, Vol. 10702, Proc. SPIE, 107020W
Salz, M., Czesla, S., Schneider, P. C., et al. 2018, A&A, 620, A97
Salz, M., Czesla, S., Schneider, P. C., & Schmitt, J. H. M. M. 2016, A&A, 586, A75
Schweitzer, A., Passegger, V. M., Cifuentes, C., et al. 2019, A&A, 625, A68
Seager, S. & Sasselov, D. D. 2000, ApJ, 537, 916
Skrutskie, M. F., Cutri, R. M., Stiening, R., et al. 2006, AJ, 131, 1163
Smette, A., Sana, H., Noll, S., et al. 2015, A&A, 576, A77
Snellen, I. A. G., de Kok, R. J., de Mooij, E. J. W., & Albrecht, S. 2010, Nature, 465, 1049
Snellen, I. A. G., de Kok, R. J., le Poole, R., Brogi, M., & Birkby, J. 2013, ApJ, 764, 182
Spake, J. J., Sing, D. K., Evans, T. M., et al. 2018, Nature, 557, 68
Suárez Mascareño, A., Rebolo, R., González Hernández, J. I., & Esposito, M. 2015, MNRAS, 452, 2745
Torres, G., Winn, J. N., & Holman, M. J. 2008, ApJ, 677, 1324
Turner, J. D., Pearson, K. A., Biddle, L. I., et al. 2016, MNRAS, 459, 789
Van Eylen, V., Agentoft, C., Lundkvist, M. S., et al. 2018, MNRAS, 479, 4786
Vidal-Madjar, A., Lecavelier des Etangs, A., Désert, J. M., et al. 2003, Nature, 422, 143
Wöllert, M. & Brandner, W. 2015, A&A, 579, A129
Wyttenbach, A., Ehrenreich, D., Lovis, C., Udry, S., & Pepe, F. 2015, A&A, 577, A62
Wyttenbach, A., Lovis, C., Ehrenreich, D., et al. 2017, A&A, 602, A36
Yee, S. W., Petigura, E. A., Fulton, B. J., et al. 2018, AJ, 155, 255
Zechmeister, M., Reiners, A., Amado, P. J., et al. 2018, A&A, 609, A12

Table 4. Physical planet parameters for GJ 3470b, HAT-P-11 b, and GJ 436 b.

Parameter	GJ 3470 b [1–5]	HAT-P-11 b [5,6]	GJ 436 b [7–10]
Host sp. type	M2.0 V	K4 V	M2.5 V
Radius [R_{Jup}]	0.36±0.01	0.389±0.005	0.374±0.009
Mass [M_{Jup}]	0.036±0.002	0.0736±0.0047	0.0728±0.0024
Density [g cm^{-3}]	1.036±0.119	1.658±0.127	1.848±0.163
T_{eq} [K]	733±23	832±10	686±10
F_{EUV} [erg s^{-1} cm^{-2}]	1435±80	2109±153	197±9
Age [Gry]	<3	6.5±5.0	6.0±5.0
He (2^3S) Absorption [%]	1.5±0.3	1.08±0.05	<0.41

References. [1]Biddle et al. (2014); [2]Kosiarek et al. (2019); [3]Dragomir et al. (2015); [4]This work; [5]Yee et al. (2018); [6]Allart et al. (2018); [7]Alonso-Floriano et al. (2015) [8]Turner et al. (2016); [9]Nortmann et al. (2018); [10]Torres et al. (2008).